Coupling light to periodic nanostructures
Driessen, E.F.C.

Chapter 8

Polarization-dependent optical absorption of superconducting single-photon detectors

We measured the single-photon detection efficiency of NbN super-conducting single photon detectors as a function of the polarization state of the incident light, for different wavelengths in the range from 488 nm to 1550 nm. The polarization contrast varies from ∼5% at 488 nm to ∼30% at 1550 nm, in good agreement with numerical calculations. We use an optical-impedance model to describe the absorption for polarization parallel to the wires of the detector. For lossy NbN films, the absorption can be kept constant by keeping the product of layer thickness and filling factor constant. As a consequence, we find that the maximum possible absorption is independent of filling factor. By illuminating the detector through the substrate, an absorption efficiency of ∼ 70% can be reached for a detector on Si or GaAs, without the need for an optical cavity.

8.1 Introduction

Superconducting single-photon detectors (SSPDs) [79], that consist of a meandering NbN wire, are an interesting new class of detectors that may outperform single-photon counting avalanche photodiodes. SSPDs feature a relatively high quantum efficiency at infrared wavelengths, combined with low time jitter, low dark counts, and high counting rates [80]. This makes these detectors promising for quantum optical studies and long-distance quantum cryptography applications [81].

A lot of attention has been given to the electronic operation of these detectors [82–84], leaving the optical design of the detectors less explored. In fact, due to the highly anisotropic nature of the wires, the detection efficiency shows a strong polarization dependence [85]. This is important, since a common way to encode quantum information is to use the polarization state of photons [86]. Detection of a photon thus comprises a simultaneous measurement of the polarization, which may be undesirable for some applications. At the same time, knowledge of the polarization dependence may simplify experimental schemes that require a polarization measurement, or can be used to optimize the detection efficiency.

The efficiency η to detect a single photon can be decomposed in an electronic and an optical contribution and can be expressed as

$$\eta = \eta_{\mathrm{e}} A, \tag{8.1}$$

where A is the optical absorption efficiency of the detector, and η_{e} is the electronic efficiency of the detector, i.e. the probability that an absorbed photon leads to a measurable voltage pulse across the detector.

The microscopic working principle of the detectors, which is essential to understand η_{e}, is still under active investigation [87, 88]. On a macroscopic level, a photon that is absorbed by the superconducting wire triggers a temporary loss of superconductivity, which gives rise to a finite voltage pulse across the detector. The optical absorption efficiency A is determined by the geometry of the detector and the dielectric constants of the substrate and the NbN layer. Since the energy of the incident photons is much larger than the superconducting gap of the NbN, the complex dielectric constant of the NbN layer at room temperature can be used.

The polarization dependence of NbN SSPDs has been investigated at a single wavelength and compared to finite-difference time domain calculations [85]. In section 8.4, we experimentally investigate the wavelength dependence of the polarization contrast, in the range between 488 and 1550 nm, and report a

strong dependence of the polarization contrast on the wavelength. We introduce an analytical optical-impedance model in section 8.5 to describe the optical absorption in thin lossy films and describe different ways to increase the detection efficiency by changing the parameters of the detector. We find that the optimum thickness is a strong function of the filling factor, while the maximum achievable absorption is independent of the NbN filling factor.

The optical impedance model also provides more insight into the cavity enhancement reported for a NbN detector inside a Fabry-Perot type cavity [85, 89]. We show, in section 8.5.3, that the absorption of the detector is enhanced by a factor n, with n the refractive index of the substrate, when the detector is illuminated from the substrate. This factor was not accounted for in earlier work and thus leads to an overestimate of the resonant enhancement. For a high index Si or GaAs substrate this factor becomes dominant and an absorption efficiencie of $\sim 70\%$ can be reached without the need for an optical cavity.

8.2 Experimental setup

The detectors in this experiment were two commercially available superconducting single-photon detectors (SSPD) [80]. These detectors nominally consist of a 4 nm thick and 100 nm wide NbN strip on an R-plane sapphire substrate, which is folded into a meandering structure of dimensions $10 \times 10 \ \mu m^2$ and filling factor 50%. Figure 8.1(a) shows a scanning electron microscope image of a detector similar to the ones used in our experiments.

SSPDs can be used to detect single photons when cooled below the critical temperature T_c of the NbN. When the detector is biased with a current close to the critical current, the absorption of a single photon deposits sufficient energy to locally bring the NbN material from the superconducting to the resistive state. The Ohmic heating due to this resistivity in turn switches a large part of the detector to the resistive state. The corresponding voltage pulse over the detector can be amplified and detected.

Figure 8.1(b) shows the electrical setup of the detectors. The dashed box shows an equivalent model circuit of the detector. It consists of a resistor of magnitude R_N in parallel with a switch. When the NbN wire is superconducting, the switch is closed. When a photon is absorbed, the switch shortly opens [83], leading to an increased impedance of the detector circuit. The inductor L_k is a model of the kinetic inductance of the superconducting wire.

Bias current I_b is provided to the detector by a voltage source V_b in series with a resistor $R_b = 400$ kΩ. Unless otherwise specified in this chapter, the
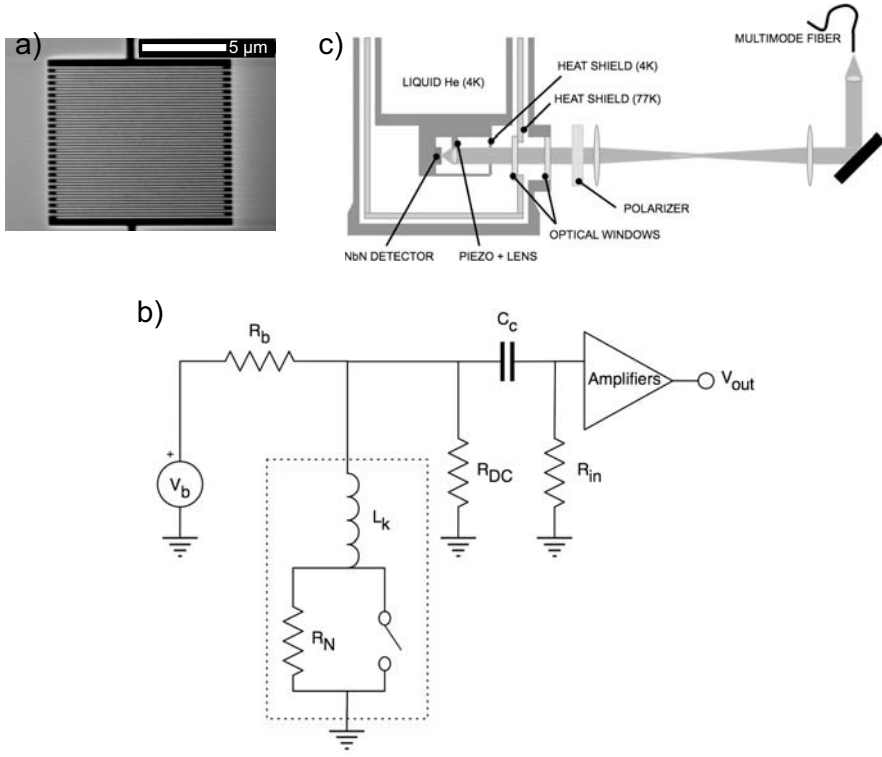
Figure 8.1. (a) SEM image of a NbN SSPD similar to the one used in the experiments. The 100 nm wide NbN line is folded into a meander with an area of $10\times10\ \mu m^2$. (b) Schematic diagram of the readout electronics. The bias current is provided by a voltage source and a resistor of 400 kΩ. The dashed box contains a phenomenologically equivalent circuit of the detector. (c) Schematic overview of the optical setup. Wavelength-filtered light from a lamp is sent through an optical fiber with a 50 μm core, and is imaged onto the detector through a telescope and a moveable lens mounted inside the cryostat.

bias current was set such that $I_b = 0.9 I_{sw}$, where I_{sw} is the current at which the detector switches to the normal state. A coupling capacitor C_c transfers the high-frequency components of the voltage pulse over the detector to a 66 dB amplifier chain[*], with an input resistance $R_{in} = 50\ \Omega$. The resistor $R_{DC} = 1\ k\Omega$ ensures that when the detector is in the normal state, the current I_b does not flow through the detector, enabling it to cool down to the superconducting

---

[*]In our experiments we used a Miteq, JS2-01000200-10-10A (gain 36 dB), amplifier, followed by a MiniCircuits ZKL-2R5 (gain 30 dB) amplifier

state. The voltage pulse V_{out} was either measured with a 1.5 GHz oscilloscope, to retrieve the pulse shape, or sent to pulse counting electronics to obtain count rates.

We mounted the SSPD in a [4]He-cryostat and cooled it to a temperature of $\sim$5 K. The temperature remained constant within 10 mK during each measurement run. Unpolarized light from an incandescent tungsten lamp was wavelength-filtered and sent through a 50 μm core size multimode optical fiber. The output of the fiber was imaged onto the detector using 4 lenses, with the final lens mounted on a piezo stage inside the cryostat, as shown in Fig. 8.1(c). The outermost two lenses form a telescope that makes a 3$\times$ demagnified image of the fiber facet on the detector. The 1:1 telescope that is formed by the middle two lenses ensures that, with a small displacement of the optical fiber, the light entering the cryostat still impinges onto the last lens. To probe the polarization dependence of the detection efficiency, a linear polarizer with an extinction ratio better than 100 : 1 for the wavelength range of interest was placed in the parallel part of the beam. To probe the wavelength dependence, we used different narrow bandpass filters ($\leq$10 nm FWHM) in combination with several edge filters to ensure that the light on the detector was monochromatic.

8.3 Characterization

Figure 8.2 shows the voltage pulse corresponding to a single detection event on the detector (dotted curve) together with an average over 100 pulses (solid curve). The initial steep rise corresponds to the detector switching to the normal state. The rise time is limited by both the 2 GHz bandwidth of the amplifier chain, and the 1.5 GHz bandwidth of the oscilloscope. After the detector switches back to the superconducting state, the voltage V_{amp} at the input of the detector is given by

$$V_{\text{amp}}(t) = R_{\text{in}}I_{\text{b}}\exp\left(-\frac{t}{\tau}\right),\qquad(8.2)$$

where τ is the reset time of the detector. The pulse shape after the detector, $V_{\text{out}}(t)$ is modified by the finite bandwidth of the amplifier chain. It is given by the convolution of the impulse response function of the amplifier chain, $H(t)$ and the voltage at the input of the detector $V_{\text{amp}}(t)$. The dash-dotted curve in Fig. 8.2 gives the best fit for τ, using the measured impulse response function of the amplifier chain, given in the inset of Fig. 8.2. This fit yields a reset time $\tau = 8.5 \pm 1$ ns.
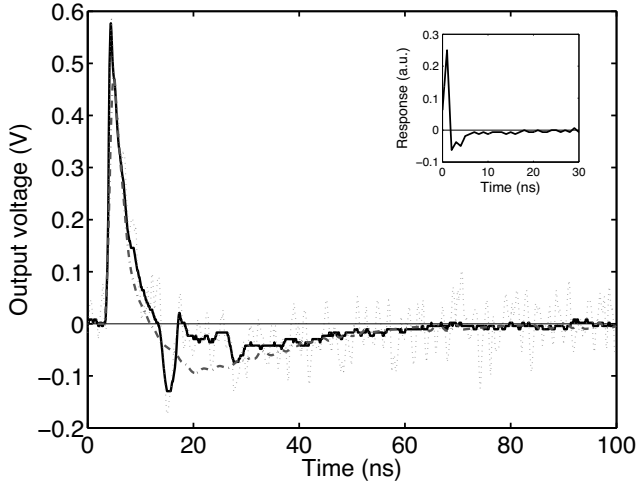
Figure 8.2. Detector pulse shape. The solid line is an average over 100 pulses. The dotted line is a single pulse, showing the noise level. The dash-dotted line is a fit to the measured pulse shape, of an exponential decay, convolved with the amplifier response shown in the inset.

The reset time of the detector should be compared to the time that is needed to restore the current through the superconducting wire, given by [83]

$$\tau = \frac{L_\mathrm{k}}{R_\mathrm{in}}. \tag{8.3}$$

From this, we determine the kinetic inductance of the detector to be $L_\mathrm{k} = 425 \pm 50$ nH, which corresponds well to the specific kinetic inductance of 0.87 nH/μm [90] for a 4 nm thick, 100 nm wide line of NbN.

In Fig. 8.3 we show the count rate of a detector as a function of the bias current I_b. When the bias current increases, less energy is needed to switch the superconductor to the normal state. This means that the probability that an absorbed photon leads to a voltage pulse increases [91]. The efficiency of the detector is ultimately limited by the optical absorption of the metal wire. The saturation of the count rate that corresponds to this limit [80] was not observed in our experiments, due to the relatively high temperature of the detectors. This indicates that $\eta_\mathrm{e} < 1$ in our measurements. The squares show the count rate when no light impinges onto the detector. The slope of this curve is comparable to the slope for an illuminated detector, indicating that the dark count rate in this case is dominated by detection of stray light, and not by the intrinsic dark count rate of the detector [92].
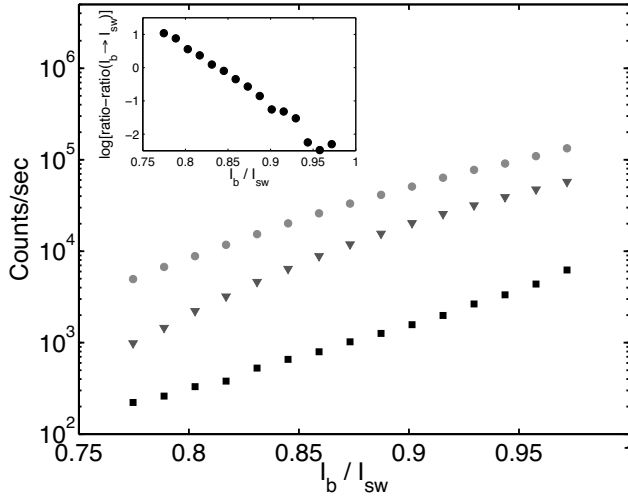
Figure 8.3. Detector count rate as a function of bias current, for light with a wavelength of 780 nm (circles) and 1550 nm (triangles). The squares show the count rate when no light impinges onto the detector. The inset shows the ratio between the count rate at 780 nm and the count rate at 1550 nm, subtracted by their ratio when $I_b \rightarrow I_{sw}$, on a logarithmic scale. Note that the absolute power impinging onto the detector was not calibrated, so that the curves at different wavelength cannot be compared directly.

The detection efficiency depends on the wavelength of the incident light as well. The circles and triangles show the count rates at a wavelength of 780 nm and 1550 nm, respectively. Although the power of the incident light was not calibrated in this experiment, it can be seen that the count rate for 1550 nm light increases more rapidly with bias current than that for 780 nm light. The ratio of these two count rates R_{780} and R_{1550}, is a single exponential

$$\frac{R_{780}}{R_{1550}} = \exp\left(-\alpha \frac{I_b}{I_{sw}}\right) + \left(\frac{R_{780}}{R_{1550}}\right)_{I_b = I_{sw}}. \qquad (8.4)$$

In the limit $I_b \rightarrow I_{sw}$, the ratio between the two curves exponentially reaches a constant value, as shown in the inset of Fig. 8.3. This behavior is not fully understood yet, although it has already been shown that it can be used to operate such a detector as a spectrometer [93].

8.4 Polarization dependence

Figure 8.4 shows the count rate of the detector as a function of linear polarization for a wavelength of 1550 nm (squares) and 532 nm (triangles). Note that the absolute count rates at different wavelengths cannot be compared directly, due to a difference in incident power. The insets show the orientation of the E-field relative to the detector. The measured count rates follow a sinusoidal dependence as a function of polarization and are minimal when the E-field is perpendicular to the lines of the detector.

We define the polarization contrast C as

$$C = \frac{N_\parallel - N_\perp}{N_\parallel + N_\perp},\tag{8.5}$$

where $N_\parallel$ and $N_\perp$ are the count rates of the detector when the light is polarized parallel and perpendicular to the wires, respectively. This definition of the contrast is a direct measure for the polarization effects, independent of the electronic quantum efficiency (η_e), and the incident power. We extract the contrast from the sinusoidal fits to the data (solid curves in Fig. 8.4). It varies with the wavelength of the incident light and is independent of the bias current and temperature of the detector in our experiment.

The circles in Fig. 8.4 show the count rate as a function of polarizer angle, at a wavelength of 1550 nm, when two wedge depolarizers under a relative angle of 45° were placed after the polarizer. These wedge depolarizers effectively depolarize the incident light by imposing a position-dependent rotation of the polarization. Indeed, the polarization contrast in this case is reduced to below 3%. The lower average count rate can be attributed to the extra four air-glass interfaces in the optical setup, leading to an increased reflection of the incident light, and can also be caused by a small displacement of the beam impinging onto the detector.

The polarization effect can be understood by comparing the periodic structure of the detector to that of a wire grid polarizer [94] that consists of a grid of parallel, highly conductive metal wires with a subwavelength spacing. For a perfect conductor the E-field should be perpendicular to the metal surface. As a consequence, only light with a polarization perpendicular to the wires is efficiently transmitted. A similar argument holds for lossy metals, albeit that in this case the field penetrates into the metal, leading to absorption. This absorption is largest when the E-field is parallel to the wires, since in this case the field penetrates more into the metal.

For the typical dimensions and spacing of the NbN wires, an effective medium approach that is accurate for both polarizations is difficult [95, 96].
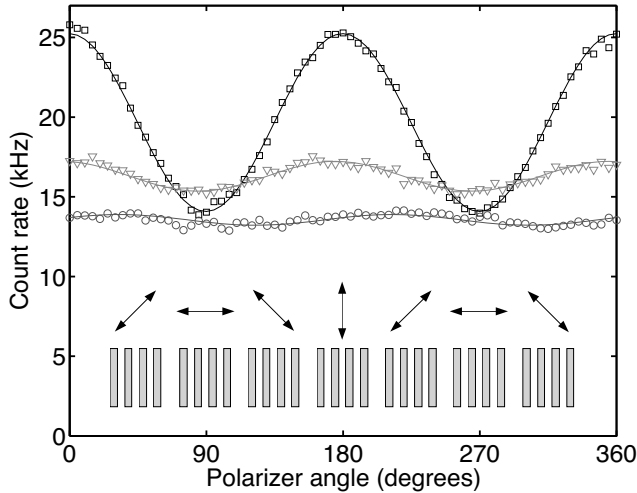
Figure 8.4. Count rate of the SSPD (corrected for stray light counts) as a function of linear polarization, for a wavelength of 1550 nm (squares) and 532 nm (triangles). The circles show the count rates for 1550 nm light when two wedge depolarizers (under a relative angle of 45°) are placed after the polarizer. The insets show the orientation of the E-field relative to the detector, for the different polarizer settings. The solid curves are sinusoidal fits to the data, used to extract the polarization contrast.

Instead, we calculated the absorption at normal incidence for an infinitely-sized detector, using the rigorous coupled-wave analysis (RCWA) developed in Ref. [37]. This method finds an exact solution of Maxwell's equations by expressing the electromagnetic fields in the different materials as a summation over all diffraction orders. The Fourier components of the periodic dielectric constant couple the diffraction orders in the patterned region. The continuity of the parallel component of the wavevector, together with the boundary conditions for the E and H fields fully determine the field in all regions. From this the intensity in all reflected and transmitted diffraction orders can be calculated. The absorption in the grating is then simply given by $A = 1 - R - T$, where R and T are the reflected and transmitted intensity.

The effects of focusing of the incident beam can be taken into account by decomposing the beam into plane waves with wave vector $\vec{k}$. Each of these plane waves will experience a different absorption $A(\vec{k})$. The effect of finite detector size can be incorporated in a similar way, by multiplying the beam profile in the near field by an aperture function $D(\vec{r})$ which is 1 at the location

of the detector, and 0 elsewhere. Taking both into account, the total absorption is given by the convolution integral

$$A = \int_{\vec{k}} A(\vec{k}) \left[u(\vec{k}) * D(\vec{k}) \right]^2 d\vec{k}, \qquad (8.6)$$

where $u(\vec{k})$ is the Fourier transform of the beam profile, and $D(\vec{k})$ is the Fourier transform of the aperture function $D(\vec{r})$.

The k-spread of the incident waves is determined by the detector size [determining the spread in $D(\vec{k})$] and the numerical aperture of the last lens in the illuminating system, determining the spread in $u(\vec{k})$. The latter is the most important factor in our experiment, since we used a large-NA lens to focus the incoming light onto the detector. Calculations of the absorption of the grating as a function of angle of incidence (i.e., as a function of $\vec{k}$) show however, that the absorption only varies appreciably from the absorption at normal incidence for angles of incidence corresponding to NA > 0.5. Therefore, the total absorption given by Eq. (8.6) can be approximated by a product of the absorption coefficient at normal incidence and the total intensity impinging on the (finite-sized) detector. This justifies the use of a plane wave calculation in the rest of this chapter.

To calculate the absorption efficiency, we used the nominal structure parameters of the detector, and tabulated values of the dielectric constant of the sapphire substrate ($n_{\text{sapphire}} = 1.74$ at 1550 nm) [97]. For the wavelength-dependent dielectric constant of NbN, a Drude model [98] was used, giving a refractive index $n_{\text{NbN}} = 5.5 + 6.3i$ at a wavelength of 1550 nm. This value is close to the value reported in Ref. [85] ($n_{\text{NbN}} = 5.23 + 5.82i$), for a thicker NbN film.

Figure 8.5(a) shows the calculated absorption for polarization parallel (TE) and perpendicular (TM) to the wires, as a function of wavelength. The absorption for parallel-polarized light monotonously increases with wavelength, whereas the absorption for perpendicular polarization goes through a maximum and decreases for wavelengths above 800 nm. This leads to a higher polarization contrast for longer wavelengths.

For comparison, the dashed curve in Fig. 8.5(a) shows the absorption of an unpatterned film, multiplied by the filling factor of NbN, as was suggested in Ref. [79]. This estimate deviates over the entire wavelength range from the polarization-averaged result obtained by RCWA, which shows that for structures with features smaller than the wavelength of light, a more refined model is needed. We will discuss this refined model in Sec. 8.5. The fact that the absorption decreases for both the parallel polarization and for the closed
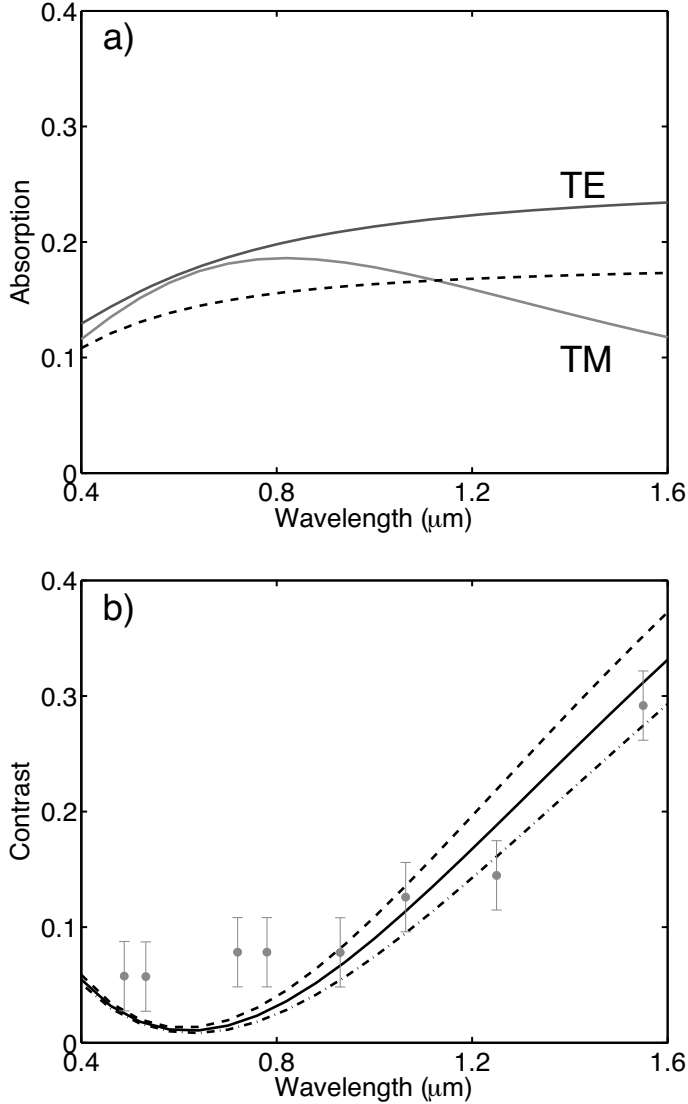
Figure 8.5. (a) Calculated absorption efficiency of a NbN grating as function of wavelength for polarization parallel (TE) and perpendicular (TM) to the lines of the detector. For comparison, the dashed line shows the calculated absorption of an unpatterned film multiplied by the filling factor of NbN. (b) Measured (dots) and calculated (black curves) polarization contrast as a function of wavelength. The calculations are shown for a filling factor of 52% (dashed), 55% (solid), and 58% (dash-dotted) and a film thickness of 4.5 nm.

film is mostly due to dispersion of the dielectric constant of the NbN material, ϵ_{NbN}.

In Fig. 8.5(b) we compare the measured polarization contrast (dots) to the results of the calculations (solid curve), as a function of wavelength. For comparison, the calculated contrast is shown for filling factors of 52% (dashed curve) and 58% (dash-dotted curve) as well. The experimentally observed contrast varies between ∼5% and ∼30% and increases with wavelength. The error bars on the experimental points represent slight variations in the measured polarization contrast during different measurement runs, as well as a slight polarization in the illuminating light source, of ∼ 1%. We attribute the fact that the calculation and the measurements differ for lower wavelengths to the fact that we used literature values for the dielectric constant of NbN. It is known that the dielectric constant of NbN varies as a function of the deposition parameters [98] and may depend on the film thickness as well [99]. Additional calculations (not shown) reveal, that for lower wavelengths, the polarization contrast is increasingly sensitive to small variations in the dielectric constant of NbN, since for these wavelengths, the Drude model for the dielectric constant of the NbN is close to resonance.

It has been shown that the linear-polarization dependence can be removed by changing the design of the detector [100]. A spiraling detector breaks the translational symmetry that causes the strong polarization contrast. The optical absorption in such a detector, however, will be lower than the maximum obtainable for parallel-polarized light, due to the fact that in these detectors, partial screening of the electric field is always possible.

8.5 Discussion

8.5.1 An optical impedance model for the absorption

In order to gain some physical insight into the absorption in the detector, we start out by describing the absorption of a film of thickness d with a complex dielectric constant ϵ_2, embedded between two dielectrics with refractive index n_1 and n_3, respectively. The film is illuminated from the medium with index n_1.

We can define the optical impedance of a medium i with refractive index n_i as

$$\eta_i = \frac{\eta_0}{n_i}, \tag{8.7}$$

where $\eta_0 = \sqrt{\mu_0/\epsilon_0} = 377 \ \Omega$ is the impedance of the vacuum. The reflection

and transmission of the layered system are given by [101]

$$R = \left| \frac{\eta_{\text{load}} - \eta_1}{\eta_{\text{load}} + \eta_1} \right|^2, \tag{8.8}$$

$$T = \frac{\eta_1}{\eta_3} \left| \frac{2\eta_{\text{load}}}{\eta_{\text{load}} + \eta_1} \right|^2, \tag{8.9}$$

where η_{load} is the combined load impedance of the film and the backing substrate. The absorption of the film is again given by $A = 1 - R - T$.

If we assume that the film is thin enough to neglect interference effects ($k_0 d \ll 1$), the load impedance is given by [102]

$$\eta_{\text{load}} \approx \frac{R_\square \eta_3}{R_\square + \eta_3}, \tag{8.10}$$

where $R_\square \approx \eta_0 / k_0 d$ Im ϵ_2 is the square resistance for a highly absorbing (Im $\epsilon_2 \gg$ Re ϵ_2) film, and k_0 is the wave vector of the light in vacuo. With these assumptions, we can write the absorption in the film as

$$A = \frac{4}{\eta_1 R_\square} \left(\frac{\eta_1 R_\square \eta_3}{\eta_1 + R_\square + \eta_3} \right)^2 = 4n_1 \frac{k_0 d \text{ Im } \epsilon_2}{(n_1 + n_3 + k_0 d \text{ Im } \epsilon_2)^2}. \tag{8.11}$$

The absorption of the film reaches a maximum value $A_{\text{max}} = n_1/(n_1 + n_3)$ for a square resistance given by

$$R_\square = \frac{\eta_1 \eta_3}{\eta_1 + \eta_3}. \tag{8.12}$$

Note that the maximum possible absorption is a function of the refractive indices of the surrounding media only. The optimal value of $R_\square$ to reach this maximum can be obtained by tuning the film thickness d.

8.5.2   The effect of film thickness

Figure 8.6 shows the absorption and the polarization contrast of a film of NbN, embedded between air ($n_1 = 1$) and sapphire ($n_3 = 1.74$), as a function of the film thickness. The solid curves show the calculated absorption using the rigorous coupled-wave analysis described before, while the dotted curves are obtained from the impedance model.

For a closed film, there is a distinct maximum of absorption, that occurs at a thickness

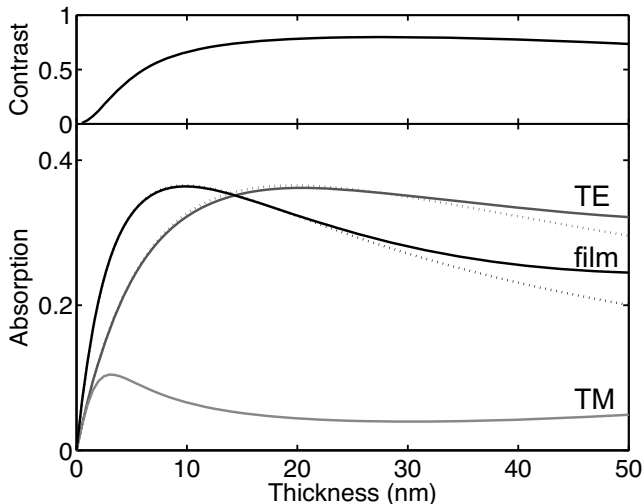$$d = \frac{n_1 + n_3}{k_0 \text{ Im } \epsilon_2}. \tag{8.13}$$

Figure 8.6. Calculated absorption at a wavelength of 1550 nm as a function of film thickness. The curve labeled "film" gives the absorption for a closed film, the other curves for a detector with lattice period 200 nm and filling factor 0.5, for polarization parallel (TE) and perpendicular (TM) to the wires of the detector. The dotted curves are calculated using the impedance model of section 8.5.1, whereas the solid curves are exact calculations using RCWA. The top graph shows the calculated polarization contrast.

For thinner films, the transmission through the film is too high to get maximal absorption, whereas for thicker films, reflection dominates.

The other curves in Fig. 8.6 show the absorption for a detector with filling factor 0.5 and lattice period 200 nm, for polarization parallel (TE) and perpendicular (TM) to the wires. The thickness for which the absorption in the patterned film is maximum, is higher than the optimal thickness for the closed film. The dotted curve is calculated using the impedance model of section 8.5.1, taking an effective dielectric constant for the absorbing film, given by [95]

$$\epsilon_{\text{eff}} = (1 - f)\epsilon_{\text{slits}} + f\epsilon_{\text{NbN}}, \qquad (8.14)$$

where f is the filling factor of the metal, and ϵ_{slits} is the dielectric constant of the material in the slits, typically air. Since only the imaginary part of ϵ_{eff} determines the absorption in the film, the absorption of the detector can simply be calculated by multiplying the thickness of the film by the filling factor. For the polarization perpendicular to the wires of the detector, it is not so straightforward to define an effective dielectric constant for the patterned

film [95, 96]. For this polarization the light is concentrated in the air slits and the effective dielectric constant is closer to that of air. Therefore the condition Im $\epsilon_2 \gg$ Re ϵ_2 used to define the impedance model, breaks down for this polarization.

Surprisingly, the calculation also shows that it is easily possible to construct a detector where the absorption for parallel polarization is larger than the absorption of an unpatterned film of the same thickness. Since the electronic efficiency of the detector, η_e, strongly depends on the thickness of the metal [103, 104], it is important to realize that the absorption for parallel-polarized light is a function of df Im ϵ_2. A reduction in thickness of the detector, to increase the electronic efficiency, can thus be countered by increasing the filling factor accordingly.

8.5.3   Illuminating through sub- or superstrate

Commonly, NbN SSPDs are deposited on a substrate of sapphire and illuminated from air. An inspection of Eq. (8.11) shows that for a certain choice of sub- and superstrate, a factor of n_3/n_1 in absorption can be gained by illuminating the detector from the medium with the higher refractive index. Figure 8.7 shows the calculated absorption for a detector, with a superstrate of air ($n_1 = 1$), as a function of the refractive index of the substrate. The thickness of the detector is set such that maximal absorption in the detector is achieved. This thickness is indicated with the line. The solid curves give the absorption for illumination from the air, whereas the dash-dotted curves give the absorption for illumination from the substrate. The different curves are for polarization parallel (TE) and perpendicular (TM) to the wires. We stress that this effect is caused by a lower impedance mismatch and should be separated from the cavity enhancement of the absorption, previously reported in Refs. [85, 89].

When the substrate index is increased, the absorption rises for illumination from the substrate side. For illumination from the air side, the absorption for parallel polarization decreases. Note however that in both cases, the polarization contrast decreases, from $C = 0.88$ at $n_3 = 1$ to $C = 0.26$ at $n_3 = 4$, and is independent on the direction of illumination, as shown in the top graph of Fig. 8.7. The absorption is a factor of n_3 higher, when the detector is illuminated from the substrate, as expected from the impedance model. It is interesting to note that, for parallel-polarized light, the absorptions from super- and substrate add up to give $A_{\text{super}} + A_{\text{sub}} \approx 1$. It is therefore possible to construct a detector with higher absorption, up to 70%, and lower polarization contrast, by using a high refractive index substrate (e.g. Si or GaAs) and illuminating
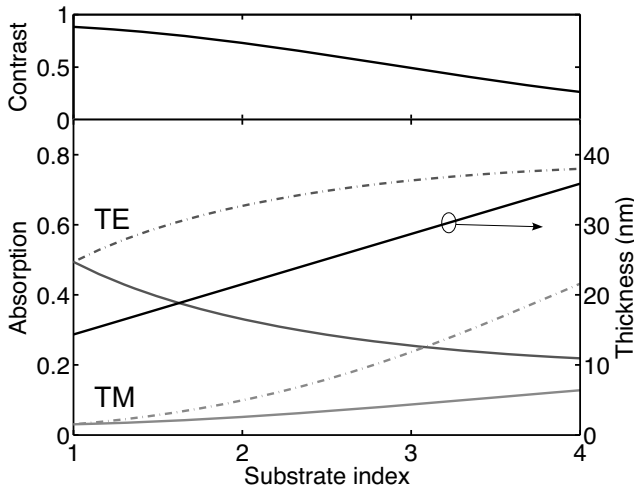
Figure 8.7. Calculated absorption for a detector with filling factor 0.5, lattice period 200 nm, at a wavelength of 1550 nm, as a function of the substrate refractive index. The solid curves are for illumination from the air side, the dash-dotted curves for illumination from the substrate side. The absorption is given for polarization parallel (TE) and perpendicular (TM) to the wires, respectively. The detector thickness is changed at each substrate index, to achieve maximal absorption. The thickness is given by the solid line (right axis). The top graph shows the polarization contrast.

the detector from the substrate. Unfortunately, increasing the refractive index of the substrate also increases the wavelength for which diffraction orders in the substrate appear. The first diffraction order at normal incidence appears at $\lambda/a = n_3$, with a the periodicity of the structure, and λ the wavelength of the light. In general, these diffraction orders lower the absorption efficiency. For a typical lattice period of 200 nm, and a substrate index of $n_3 = 3.5$, the first diffraction order appears at a wavelength of 700 nm, making detectors on a high-refractive-index substrate less effective for detecting visible light. The problem of diffraction could also be circumvented by designing a detector that has a variable line spacing.

8.6   Conclusion

In conclusion, we have measured a polarization dependence in the detection efficiency of NbN superconducting single photon detectors and find a wave-

length dependent polarization contrast between 5% and 30%. This effect can be explained by the geometry of the detector. Calculations of the optical absorption efficiency give good agreement with the measured data. We have demonstrated that the polarization dependence can be removed by the use of wedge depolarizers.

Furthermore, we have shown that the parameters of the detector can be tuned to achieve an absorption for a polarization parallel to the detector wires, that exceeds the absorption of an unpatterned film of the same thickness. We have given a simple optical impedance model, that allows for a quick estimate of the parameters needed to optimize the detector. For parallel-polarized light, the maximum absorption achievable is not determined by the thickness or the dielectric constant of the metal film, nor by the filling factor, but only by the refractive indices of the surrounding media. We have shown that by illuminating the detector from the substrate it is possible to increase the detection efficiency of the detector even further, by a factor equal to the refractive index of the substrate. Such highly absorbing, highly polarization-dependent detectors can be employed to efficiently detect photons with a well-defined polarization.

94